Multi-Responsive Emissions in Luminescent Ions Doped Quaternary Piezophotonic

Materials for Mechanical-to-Optical Energy Conversion and Sensing Applications

Yingjie Zhao, Dengfeng Peng, Gongxun Bai*, Youqiang Huang, Shiqing Xu*, Jianhua Hao*

Y. J. Zhao, Y. Q. Huang

College of Materials and Chemistry,

China Jiliang University (CJLU)

Hangzhou 310018, People's Republic of China

Prof. D. F. Peng

College of Physics and Optoelectronic Engineering

Shenzhen University (SZU)

Shenzhen 518060, People's Republic of China

E-mail: pengdengfeng@szu.edu.cn

Prof. G. X. Bai, Prof. S. Q. Xu

Institute of Optoelectronic Materials and Devices

China Jiliang University (CJLU)

Hangzhou 310018, People's Republic of China

E-mail: baigx@cjlu.edu.cn, shiqingxu@cjlu.edu.cn

Prof. J. H. Hao

Department of Applied Physics

The Hong Kong Polytechnic University (PolyU)

Hong Kong, People's Republic of China

E-mail: jh.hao@polyu.edu.hk

Keywords: piezophotonics, mechanoluminescence, luminescent ions, pressure distribution, energy conversion

Visualization and non-contact sensing can be achieved based on multimode luminescent materials, which is essential to flexible optoelectronics, information encryption, and infrastructure monitoring. However, the development of optical sensors is primally limited by developing high-performance luminescent functional materials with energy conversion. Here, by co-doping transition metal and lanthanide ions into quaternary piezophotonic semiconductors MZnOS (M=Ca, Sr, Ba) microcrystals, the efficient multimode luminescent materials are successfully synthesized. They can simultaneously respond to ultraviolet, near-infrared and stress, and exhibit completely different optical characteristics. Specifically, both composite film and block have been prepared by mixing luminescent particles and polymers for mechanical-to-optical energy conversion. The developed composite based on mechanoluminescence can be utilized for visualizing pressure distribution, even E-signature, and anti-counterfeiting systems. In addition, the temperature detection has been researched based on upconversion emissions. The results suggest that these materials have great potential applications in advanced optical multi-mode sensors, which is of significance for integrated optoelectronic devices.

1. Introduction

Luminescent materials have been widely researched due to their fascinating physics and extensive applications.[1-3] According to the diverse excite sources, the types of luminescence can be classified as electroluminescence (EL), photoluminescence (PL), mechanoluminescence (ML), thermo-luminescence (TL), and even magnetic-induced luminescence (MIL), and so on.[4-8] Multimode luminescent materials that display photon emissions in response to various excitations are significant for the applications such as flexible optoelectronics, bioimaging, information encryption, memory, and optical sensors.[9-15] Especially, it is highly pivotal for multifunctional sensing to achieve multi-stimuli responsive luminescence such as human-

machine interfaces, multiple strains and magnetic fields sensing.[16-20] Due to the convenience of molecular design, organic fluorescent dyes have many advantages in realizing multi-responsive emissions. By integrating different functional units or using molecule interactions, organic dyes have been confirmed to possess multiple luminescence forms including ML, persistent luminescence, PL.[21-23] However, organic dye molecules have the poor chemical stability because of their fragile molecular structures. Composite materials can also emit multimode luminescence by mixing different luminescent materials together, but they always have the lower luminous efficiency due to the incompatibility.[10,14] Despite great success in the past decade, the development of multimode luminescent technologies still faces serious challenges in constructing a suitable multimode light-emitting structure. As a substitute for composite materials and organic dyes, impurity-doped luminescent materials have been regarded as a promising new type of multimode emitters. What's more, they are single-component inorganic materials, which means the stable structures and the higher luminous efficiency.[11,18]

Compared to the extensive researches of upconversion and down-shifting luminescence, the investigation of the ML is relatively rare in multimode luminescent material.[17,19] Notably, Xu et al. reported the pioneering works that the intense visible emissions can be emitted from some materials under mechanical stimuli. For instance, the representative $ZnS:Mn^{2+}$ and $SrAl_2O_4:Eu^{2+}$.[13,15] It has aroused widespread attention from researchers. However, for a long time, the mechanism behind ML phenomenon has lacked scientific and reasonable explanations. It seriously hinders the development of ML materials. For the better understanding, Wang proposed the concept of piezophotonics, which can be treated as a two-way coupling between piezoelectricity and photoexcitation properties.[24-26] There are many typical piezoelectric materials such as binary ZnS, ZnO, GaN, InN and ternary piezoelectric materials $Pb(Zr,Ti)O_3$, $LiNbO_3$. It is worth noting that these materials have achieved tremendous success in the field

of piezophotonics in the past decade. However, it is difficult to meet the needs of multi-mode luminescence because of their single doping site. For example, ZnS is only compatible with metal ions (Mn, Cu, Al, etc.) and not with lanthanide elements.

Meanwhile, the quaternary piezophotonic materials MZnOS (M=Ca, Sr, Ba) have two types of cation sites M^{2+} and Zn^{2+}, which can accommodate lanthanide and transition metal ions, respectively. Besides, they are all wide-bandgap semiconductors, it means their optical properties can be easily modulated by the dopant levels. The quaternary piezoelectric materials were chosen as the host materials in our research because of their capability to efficiently realize mechanical-to-optical energy conversion and offer the flexibility for impurity doping.[14,16] Single-doped CaZnOS has been proven to have excellent photoelectric properties.[10,27] However, there is a lack of corresponding research on multi-doping based multimode luminescence for quaternary piezophotonic semiconductors MZnOS (M= Sr, Ba, Ca). In this work, by codoping transition metal and lanthanide ions into the cation vacancies of quaternary piezophotonic materials, numerous trap levels can be established between the conduction and valance bands, causing highly designable luminescence processes upon different excitation conditions. Here, we systematically investigate the multimode luminescence based on quaternary piezophotonic materials codoped with manganese (II) and lanthanide (III) ions. The multifunctional sensing based on multimode luminescence is further characterized, which is significant for integrated optoelectronic applications.

2. Results and discussion

2.1. Crystal structure and morphology
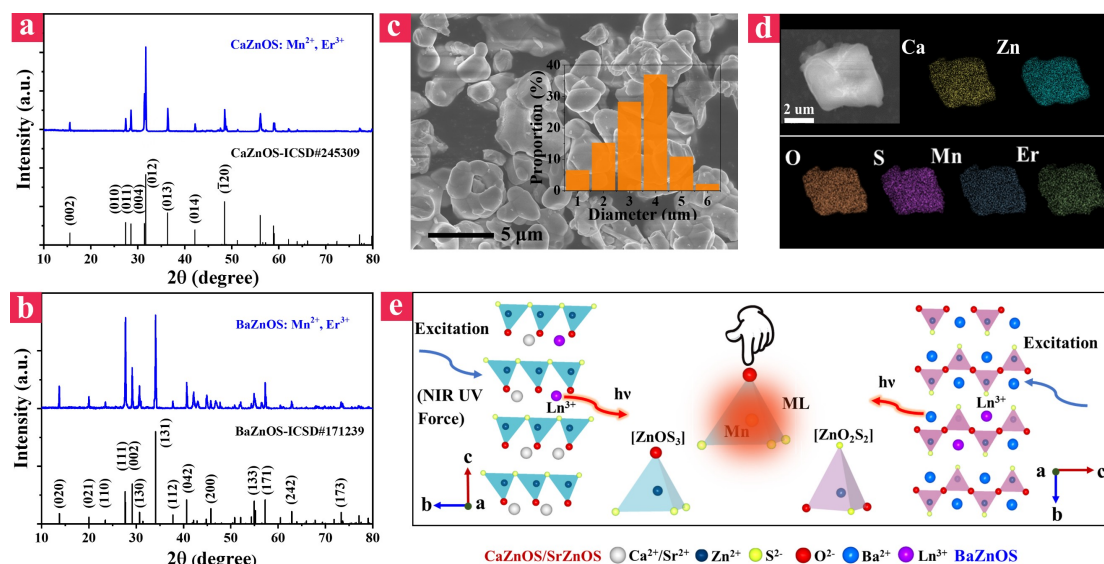
Figure 1. The crystal structure and morphological characterizations. (a) and (b) The XRD patterns of CaZnOS:Mn^{2+}/Er^{3+} and BaZnOS:Mn^{2+}/Er^{3+} samples. (c) The SEM image of CaZnOS:Mn^{2+}/Er^{3+} particles. The inset presents the bar charts of the size distribution. (d) The EDS mapping of an individual CaZnOS:Mn^{2+}/Er^{3+} microcrystal. (e) The crystal structures and luminescence mechanism of Mn^{2+}/Ln^{3+} codoped MZnOS (M=Ca, Sr, Ba).

The crystal structure and morphology play a critical role in the physical properties of materials, the XRD and SEM measurements have been utilized to investigate the as-prepared samples. As shown in Figure 1a and b, the diffraction information of the CaZnOS:Mn^{2+}/Er^{3+} and BaZnOS:Mn^{2+}/Er^{3+} crystals matches well with the standard Inorganic Crystal Structure Database cards (ICSD #245309, ICSD #171239). Meanwhile, the XRD pattern of prepared SrZnOS:Mn^{2+}/Er^{3+} sample and the theoretical pattern (ICSD #431819) were also provided (Figure S1, Supporting Information). These results show that the prepared samples have a high crystallinity. The patterns of the as-prepared CaZnOS:Mn^{2+}/Er^{3+} sample show a little shift, compared with the standard data. It is deduced that Mn^{2+}/Er^{3+} ions enter the lattice of the CaZnOS host, leading to a slight change in the crystal lattice. The morphology of the CaZnOS:Mn^{2+}/Er^{3+} sample was characterized by SEM, as shown in Figure 1c. The inset presents that the particle size distribution of the microcrystals is mainly about 2-5 μm. Figure

5

1d shows the EDS mapping of an individual $CaZnOS:Mn^{2+}/Er^{3+}$ particle. It can be clearly seen that the distribution of various elements is homogeneous in the particle. It means that the lanthanide Er and transition metal Mn have been successfully doped into the CaZnOS microcrystals. We choose quaternary piezoelectric semiconductors MZnOS (M=Ca, Sr, Ba) as the hosts in our research due to their effective ML property and the convenience for ions doping. There are two types of cation sites contained in MZnOS (M=Ca, Sr, Ba) hosts, namely M^{2+} (Ca^{2+}=0.10 nm, Sr^{2+}=0.11 nm, Ba^{2+}=0.14 nm,) and Zn^{2+} (0.07 nm). Figure 1e shows the crystal structures and luminescence mechanism of Mn^{2+}/Ln^{3+} codoped MZnOS (M=Ca, Sr, Ba), the lanthanide ions Er^{3+} (0.09 nm) and transition metal ions Mn^{2+} (0.08 nm) mainly enter the $Ca^{2+}/Sr^{2+}/Ba^{2+}$ and Zn^{2+} sites, respectively.[27] However, the strict control of synthetic conditions is necessary for preparing the doped quaternary piezoelectric materials. MZnOS polycrystals are commonly synthesized in a narrow temperature range.[28] When the temperature is too high, they have a weight loss due to the melt and decomposition of the eutectic.[29] It is usually small that the number of lanthanide ions which can enter the lattice of CaZnOS (< 2%), due to the finite reactivity of lanthanide precursors in the moderate reaction temperature range.[16] These three quaternary piezophotonic materials MZnOS (M=Ca, Sr, Ba) all possess the layered crystal structure, which can effectively separate and transport electron-hole pairs, making it a suitable host lattice for generating intense photon emission under external mechanical stimuli.[30,31] In general, the crystal parameters can determine the optical properties of the material. Among them, CaZnOS adopts a polar, non-centrosymmetric, hexagonal crystal structure ($P6_3mc$, a=3.75726 Å and c=11.4013 Å) and is isostructural to SrZnOS ($P6_3mc$, a=3.90442 Å and c=11.6192 Å).[32,33] It aroused the similar optical properties of these two materials. However, BaZnOS crystallizes in a centro-symmetric, orthorhombic crystal structure (Cmcm, a=3.9619 Å, b=12.8541 Å, c=6.1175 Å), which is quite different with CaZnOS and SrZnOS.[34] The high symmetry of the crystal structure is usually unfavorable for the piezophotonic effect. However, $BaZnOS:Mn^{2+}/Er^{3+}$ with a high symmetry crystal structure

still has the intense ML, which is considered to be related to the local piezoelectric field near the luminescent ions in the host lattice rather than bulk piezoelectricity.[35] It is worth noting that CaZnOS and SrZnOS are composed of parallel-arranged tetrahedra [ZnOS$_3$] units separated by Ca/Sr ions. BaZnOS is consist of vertex-linked [ZnO$_2$S$_2$] tetrahedra units separated by Ba ions.[26] And it is similar to [ZnOS$_3$] in CaZnOS and SrZnOS. For ML, the tetrahedron unit is the effective crystal structure to achieve energy conversion. Here, Mn^{2+} ions would enter [ZnOS$_3$] and [ZnO$_2$S$_2$] tetrahedral units.[27] It can be used to explain that why the Mn^{2+} doped CaZnOS has a higher ML efficiency than that Ln^{3+} doped MZnOS (M=Ca, Sr, Ba). And the tetrahedral [ZnOS$_3$] units have a high degree of asymmetry than [ZnO$_2$S$_2$].
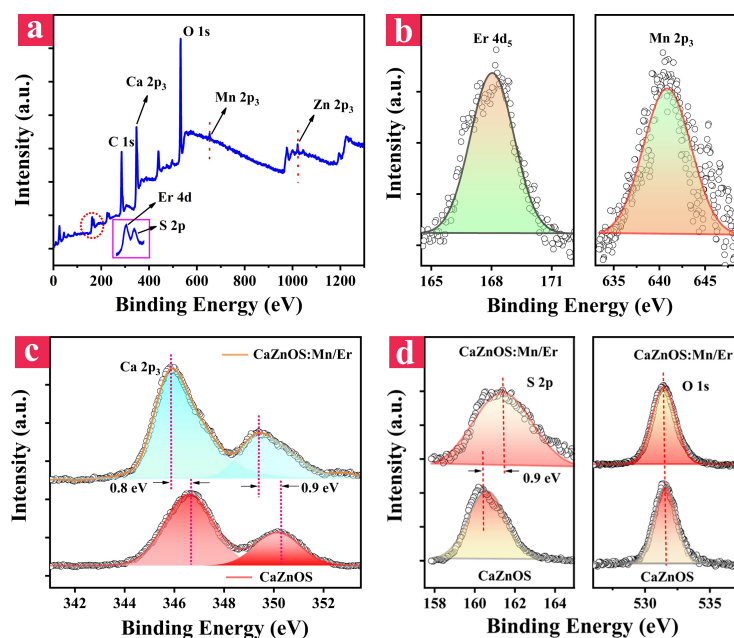

Figure 2. The XPS spectra of the CaZnOS:Mn^{2+}/Er^{3+} sample. (a) The full elements scanning XPS. (b) The fitted XPS spectra of Er 4d$_5$ and Mn 2p$_3$. (c) The spectra of Ca 2p$_3$ in doped and undoped CaZnOS samples. (d) The spectra of S 2p and O 1s in doped and undoped CaZnOS.

The chemical element analysis of the CaZnOS:Mn^{2+}/Er^{3+} sample was implemented using XPS measurements. According to the binding energy of the sample, XPS can validate the delicate changes in the chemical microenvironment, such as element, valence, and structure. In the range from 0 to 1350 eV, the binding energy peaks of all elements in the sample have been

observed in Figure 2a. As depicted in Figure 2b, the characteristic peak corresponding to Er $4d_5$ core-level at 168 eV is detected in the sample. It matches well with the formerly reported XPS features in the $ErSi_{1.7}$ sample (Er 4d, 168 eV) and MoS_2:Er thin films (Er 4d, 168 eV).[36-38] At the same time, the obvious binding energy peak corresponding to Mn $2p_3$ core-level at 641 eV was also detected in the sample. And it matches well with the XPS data from the $Mn_{0.09}Cu_{0.81}Ce_{0.05}Zr_{0.05}O_{2-\delta}$ sample (Mn 2p, 641 eV).[39] Moreover, the peak centered at 641 eV is assigned to the Mn^{2+} species, showing that Mn^{2+} is presented in the sample.[40,41] Figure 2c illustrates the Ca 2p spectra of the doped and undoped samples. The asymmetrical spectra have been fitted into two resolved peaks by the Gaussian-Lorentzian deconvolution. Compared with the undoped sample, the predominant peak in the doped one centered at 346 and 349 eV have experienced left shifts of 0.8 and 0.9 eV, respectively. Notably, the left chemical shift means that the chemical binding energy becomes lower. The chemical binding energy difference is contributed by the Fermi level shift, which is an obviously evidence that the dopant has been successfully doped into the crystal lattice. For S 2p spectra in Figure 2d, it can be found that the doped sample has a broader peak around 161.4 eV than the undoped one. It means the higher chemical binding energy is caused by potential oxidation reactions in the air. The O 1s spectra are shown in Figure 2d, the peaks have no clearly chemical shift or change, due to that the dopants do not occupy O lattice site here. The XPS results show that the prepared $CaZnOS:Mn^{2+}/Er^{3+}$ sample contains the elements of Ca, Zn, O, S, Mn, and Er. Luminescent ions Mn^{2+} and Er^{3+} have been successfully introduced into the CaZnOS host.

2.2. PL spectroscopic study
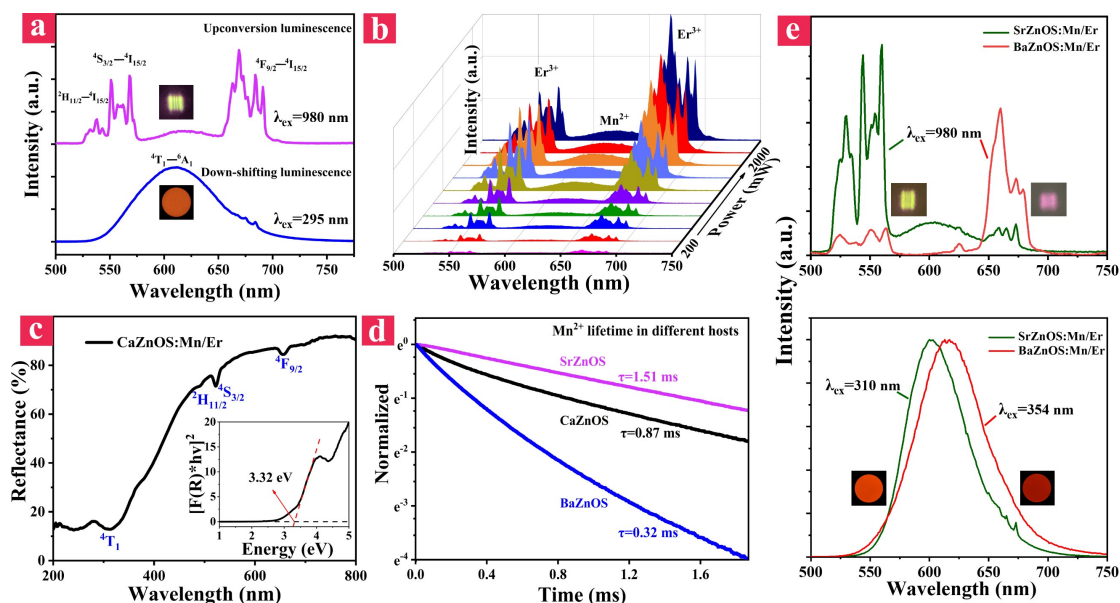
Figure 3. The PL performance of the samples. (a) The upconversion, down-shifting spectra of the doped CaZnOS. Inset: optical images under near-infrared laser (upper) and ultraviolet (lower) excitation. (b) Upconversion luminescent spectra of the doped CaZnOS under a 980 nm laser with increasing power. (c) The diffuse reflectance spectrum of doped CaZnOS sample. The inset depicts the Tauc plot and the calculated band gap. (d) PL decay curves of Mn^{2+} in $MZnOS:Mn^{2+}/Er^{3+}$ (M=Ca, Sr, Ba) samples. (e) The upconversion, down-shifting spectra of $SrZnOS:Mn^{2+}/Er^{3+}$ and $BaZnOS:Mn^{2+}/Er^{3+}$ samples. Inset: their optical images under 980 and 254 nm excitation.

The PL spectra of as-synthesized samples are presented in Figure 3. The sample simultaneously possesses upconversion and down-shifting luminescence properties, which are mainly contributed by Er^{3+} and Mn^{2+} ions, respectively. Figure 3a illustrates the comparison between the two types of PL spectra from $CaZnOS:Mn^{2+}/Er^{3+}$ samples. The upconversion emission spectrum is primally generated from the luminescent centers Er^{3+} ions. There are two primary green emissions centered at 530 and 550 nm as well as a red peak located at 670 nm, which can be assigned to $^2H_{11/2}$, $^4S_{3/2}$, $^4F_{9/2} \rightarrow ^4I_{15/2}$ transitions of Er^{3+} under the excitation of 980 nm laser, respectively. The down-shifting emission spectrum is mainly produced from the luminescent centers Mn^{2+} ions in the sample. There is an intense orange luminescent peak centered at 610 nm under the excitation of ultraviolet (UV) resource 295 nm. The orange peak can be assigned to the $^4T_1 \rightarrow ^6A_1$ transition of Mn^{2+} ions.[42,43] And it almost covered the down-conversion

9

luminescence of Er^{3+} ions in this matrix.[44] Besides, the images of the $CaZnOS:Mn^{2+}/Er^{3+}$ disk are presented in Figure 3a, under 980 nm laser and 254 nm UV light, respectively. In Figure 3e, $SrZnOS:Mn^{2+}/Er^{3+}$ also shows intense green emission by the excitation of 980 nm light source, but the difference is that the $BaZnOS:Mn^{2+}/Er^{3+}$ presents a strong red fluorescence. The same luminescent ions may generate different light emission in different hosts, which is may influenced by the factors such as coordination environment, lattice parameters, crystal orientation, and so on.[4,45] Here, the phenomenon of the multi-color emission is caused by the variation of the relative luminescent intensity of the red and green emissions of Er^{3+} ions in the three compounds. It can be mainly attributed to the different crystal fields of the three matrixes. Meanwhile, the optical images of $SrZnOS:Mn^{2+}/Er^{3+}$ and $BaZnOS:Mn^{2+}/Er^{3+}$ disks are presented, under 980 nm laser and 254 nm UV light, respectively. The color change in different situations gives these materials a potential application for anti-counterfeiting and indication. The excitation power dependent upconversion emission spectra of the sample are further researched under the different pump power. Figure 3b illustrates the upconversion emission spectra of $CaZnOS:Mn^{2+}/Er^{3+}$ sample under 980 nm laser excitation with the pump power from 200 to 2000 mW. As the pump power increases, the relative intensity of the red peak from Er^{3+} ions increases faster than the green emission peaks. The $SrZnOS:Mn^{2+}/Er^{3+}$ and $BaZnOS:Mn^{2+}/Er^{3+}$ samples also show this trend (Figure S2, Supporting Information). Besides, the gradually increasing emission peak located at 610 nm of Mn^{2+} can be also observed, which is caused by the energy transfer from Er^{3+} ions. Figure 3c shows the diffuse reflectance spectrum of the $CaZnOS:Mn^{2+}/Er^{3+}$ in the spectral region of 200-800 nm. The optical band gap of the sample is evaluated to be 3.32 eV according to the Kubelka-Munk method and Tauc plot (inset of Figure 3c). It is similar to the calculated band gap of $SrZnOS:Mn^{2+}/Er^{3+}$ (3.11 eV) and $BaZnOS:Mn^{2+}/Er^{3+}$ (3.31 eV) samples (Figure S3, Supporting Information). These three doped piezophotonic materials all have a wide band gap, which means their optical properties can be easily modulated by the dopant levels. Figure 3d illustrates the down-shifting emission lifetime

profiles of Mn^{2+} in $MZnOS:Mn^{2+}/Er^{3+}$ (M=Ca, Sr, Ba), which are 0.87, 1.51 and 0.32 ms, respectively. Decay curves of Er^{3+} upconversion emission at 530, 550, and 670 nm under excitation at 980 nm laser are also carefully investigated (Figure S4, Supporting Information). In ML semiconductors, the shorter lifetime of the luminescent center is more suitable for the dynamic stress sensing. The specific data emerge in Table 1. As we know, the asymmetric structure and lattice parameters play an important role in optoelectronic properties.[4] The crystal structure of BaZnOS has higher symmetry, and the lattice parameters of SrZnOS are larger than that of CaZnOS. Therefore, the differences in crystal structure and lattice parameters among CaZnOS, BaZnOS and SrZnOS samples lead to diverse luminescent properties.

Table 1. Quaternary piezophotonic semiconductors and their properties.

| Composition	Crystal system	Mn^{2+} Lifetime (ms)	Band gap (eV)	Down-shifting center (nm)	ML center (nm)	Response pressure (MPa)
CaZnOS:Mn/Er	Hexagonal	0.87	3.32	610	610	0.73
BaZnOS:Mn/Er	orthorhombic	0.32	3.31	616	590	1.15
SrZnOS:Mn/Er	Hexagonal	1.51	3.11	602	602	0.91

2.3. Pressure sensing
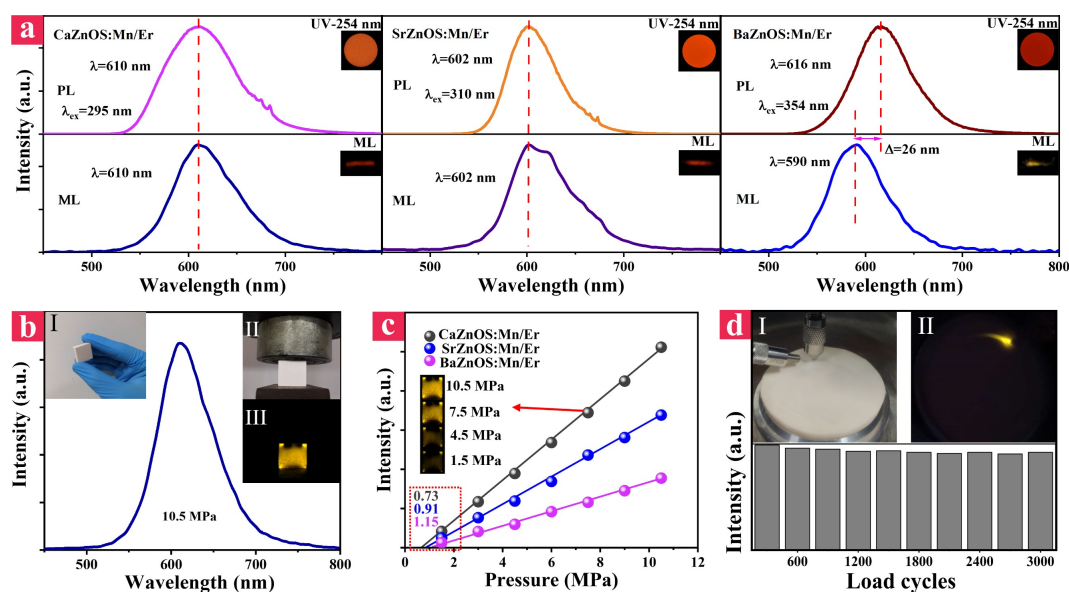
Figure 4. (a) The PL (top) and ML (bottom) spectra of MZnOS:Mn^{2+}/Er^{3+} (M=Ca, Sr Ba) powders. The insets present optical images of samples under 254 nm UV excitation and upon rubbing by a glass rod. (b) The ML spectrum of the CaZnOS:Mn^{2+}/Er^{3+} composite block under the maximum pressure of 10.5 MPa. Inset: (I) An image of the prepared composite block sample. (II) The photo of the composite block in the material testing machine. (III) A photo of the piezoluminescence from the sample during 10.5 MPa compressive load in the dark field. (c) The ML responses of MZnOS:Mn^{2+}/Er^{3+} (M=Ca, Sr, Ba) composite blocks, showing the linear relationship between the intensity and loaded pressure (1.5-10.5 MPa). Inset: optical images of the CaZnOS:Mn^{2+}/Er^{3+} sample under different compressive load in the dark field. (d) The CaZnOS:Mn^{2+}/Er^{3+} sample in the rubbing test system and the cycle stability tests.

The ML performance of the prepared quaternary piezoelectric materials has been developed for mechanical-to-optical energy conversion and optical sensing. The CaZnOS:Mn^{2+}/Er^{3+} and SrZnOS:Mn^{2+}/Er^{3+} powders present orange emission peaked at 610 and 602 nm upon mechanical stimulus, which is similar to their PL spectra. However, compared with the PL spectrum, the ML of BaZnOS:Mn^{2+}/Er^{3+} exhibits a blue shift of 26 nm. It is deduced that the ML is generated from the deeper traps in the sample.[28,46] For recording relatively large pressure, the ML composite block was fabricated by mixing the ML microcrystals and epoxy resin (Inset I in Figure 4b). Inset II and III indicate the contrastive photos of the composite block sample before and during the compression. Especially, Inset III illustrates the piezoluminescent image of the composite block during an applied pressure of 10.5 MPa utilizing the material test machine in the dark environment. Meanwhile, Figure 4b presents the ML spectrum of the CaZnOS:Mn^{2+}/Er^{3+} composite block under the maximum pressure of 10.5 MPa, which is similar to the ML spectrum of the composite film. With the applications of repeated loads to the block, highly reproducible ML can be observed in the dark field without excitations of additional energy such as UV source (Video S1, Supporting Information). In the elastic range, Figure 4c presents a comparison of ML response for MZnOS:Mn^{2+}/Er^{3+} (M = Ca, Sr, Ba) composite blocks under a compressive load. According to the experimental piezoluminescent

intensity, the stress distribution of the composite blocks can be analyzed. And they all showed the linear relationship between intensity and applied pressure (1.5-10.5 MPa). Take the CaZnOS:Mn^{2+}/Er^{3+} for example, the fitted equation is as follows:

$$ML\text{-}Intensity = 3.1\xi\,Pressure - 2.7 \qquad (1)$$

The fitting quality is high ($R^2 = 0.992$). Notably, the ML intensity is normalized here, so it is the arbitrary unit (a.u.). According to the equation, the response threshold of this sensor is estimated to be 0.73 MPa. And the response pressure of other blocks is listed in Table 1. For pressure sensing, compared with many existing ML materials, many of them require charging from external excitation sources, such as $BaSi_2O_2N_2$:Eu^{2+}/Dy^{3+}, $La_{1.95}Ti_2O_7$:Pr^{3+}, and $Sr_3Al_2O_6$:Eu^{3+}.[46-48] It seriously hinders the practical applications in pressure sensing. The quaternary piezophotonic materials doped with Mn/Er not only have self-recoverable ML but also have a low response threshold, which means the higher sensing sensitivity. The slope demonstrates the sensitivity of the device response to the pressure. The inset in Figure 4c shows the corresponding ML images of the composite block under different compressive loads. Figure 4d depicts that the excellent ML stability of the CaZnOS:Mn^{2+}/Er^{3+} composite disk even after rubbing quickly 3000 times. The rubbing test platform is shown in inset I of Figure 4d, the inset II shows the ML image of the sample during the test. The applied force is fixed at 3.0 N. The tests suggest that the CaZnOS:Mn^{2+}/Er^{3+} composite disk has a good ML repeatability. These quaternary piezoelectric semiconductors and their luminescent properties are summarized in Table 1. Among the three compositions, the CaZnOS:Mn^{2+}/Er^{3+} possesses the most sensitive ML and the largest band gap.
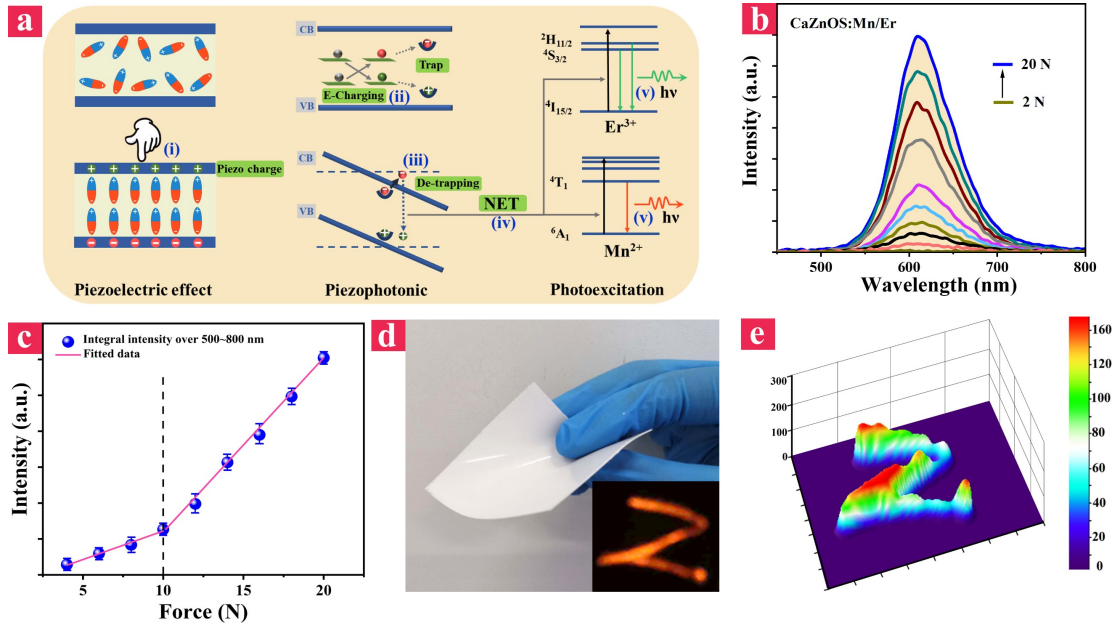
Figure 5. The mechanism of piezophotonic effect and mechanical-to-optical characteristics of the composite film. (a) Energy transfer schematic presenting the piezophotonic effect-initiated luminescence in Mn/Er codoped quaternary piezophotonic materials. (i) Stress-induced piezo charge and piezopotential in piezoelectric crystal. (ii) Electrons and holes are captured by traps. Electric-field induced charge-separation (E-charging). (iii) Detrapping of electrons is promoted due to tilting of energy bands under stress-induced piezopotential. (iv) Nonradiative energy transfer (NET) to excite luminescent ions. (v) Excited luminescent ions fall back to ground state with the light emission. (b) ML spectra under various applied forces. (c) Integral intensity versus different applied forces in the composite film. (d) Flexible composite film fabricated by mixing ML powder and PDMS. Inset: visualization of handwriting track by long-time exposure imaging on the composite film. (e) The distribution of relative ML intensity in the handwriting trajectory analyzed from ML photo in the inset of (d) according to the grayscale value.

It is worth noting that the quaternary piezophotonic materials have the excellent ML strength and repeatability. The deep mechanism behind them can be explained by the piezophotonic effect, which is a two-way coupling effect between piezoelectricity and photoexcitation features.[6,7] Here, the proposed energy conversion processes are schematically illustrated in Figure 5a. (i) Under the external mechanical stimuli，the centers of piezoelectric crystal are

14

slightly separated along a certain direction, creating a dipole moment.[14] Then the piezo charge and piezopotential are produced in the piezo crystal. (ii) The neutral defect centers are separated into electrons and holes due to the electric-field. Subsequently, they are captured by traps near the conduction band (CB) and valence band (VB), respectively. (iii) The piezopotential in crystal tilts the energy bands, so that the captured electrons can then escape from traps. (iv) The nonradiative recombination of electrons and holes released energy, followed by transfer to the luminescent ions for exciting them from the ground state to excited state. (v) Finally, when the excited luminescent ions fall back to the ground state, the photon emission occurs.[27] For the purpose of detecting the distribution of applied force or visualizing the pressure, a flexible composite film is synthesized. It contains the uniform layer of $CaZnOS:Mn^{2+}/Er^{3+}$ and PDMS mixture, which sealed by PET films. The ML characters of the film are carefully researched by applying different loaded forces on it. As demonstrated in Figure 5b, the typical ML spectra can be extracted from the film upon a series of applied forces, showing a fixed peak located at 610 nm. For comparing the ML performance of the three samples, the ML spectra of $SrZnOS:Mn^{2+}/Er^{3+}$ and $BaZnOS:Mn^{2+}/Er^{3+}$ composite films were also recorded (Figure S5, Supporting Information). In Figure 5c, the integral intensity of the ML for each applied pressure in the range from 2 to 20 N was summarized. It indicates that the ML emission intensity increases with loaded forces, which presents a linear dependence. The slope of the curve can be defined as the sensitivity of the ML film for force/strain sensing.[49] Notably, the ML intensity shows a clear linearly increasing tendency within the range of 10-20 N. For the pressure-induced ML, the distortion of host lattice emerges with increasing applied forces. It induces the rapid variation in the piezoelectric potential of the matrix, hence resulting in the rapid growth of the ML intensity.[50] Meanwhile, the ML under relatively low strength of force (<10 N) is mainly attributed to the triboelectric effect, which is an effect caused by the frictional contact between ML particles and packing PET films induce tribocharge at the contact surface.[51] By parallel reading out of the location and intensity of light emissions introduced

through the ML process of the film, the position and the magnitude of forces can be precisely sensed. The inset in Figure 5d was recorded in the dark field by a digital camera in the long exposure mode. It demonstrates visualization of a 2D pressure image by capturing a handwritten character "Z". The relative ML intensity of the handwriting trajectory was derived and illustrated in Figure 5e by analyzing the grayscale of the optical image "Z". The significance of this work lies in the people's writing characteristics can be analyzed by extracting the gray value of ML images, so as to achieve the purpose of E-signature and anti-counterfeiting.

2.4. Temperature sensing
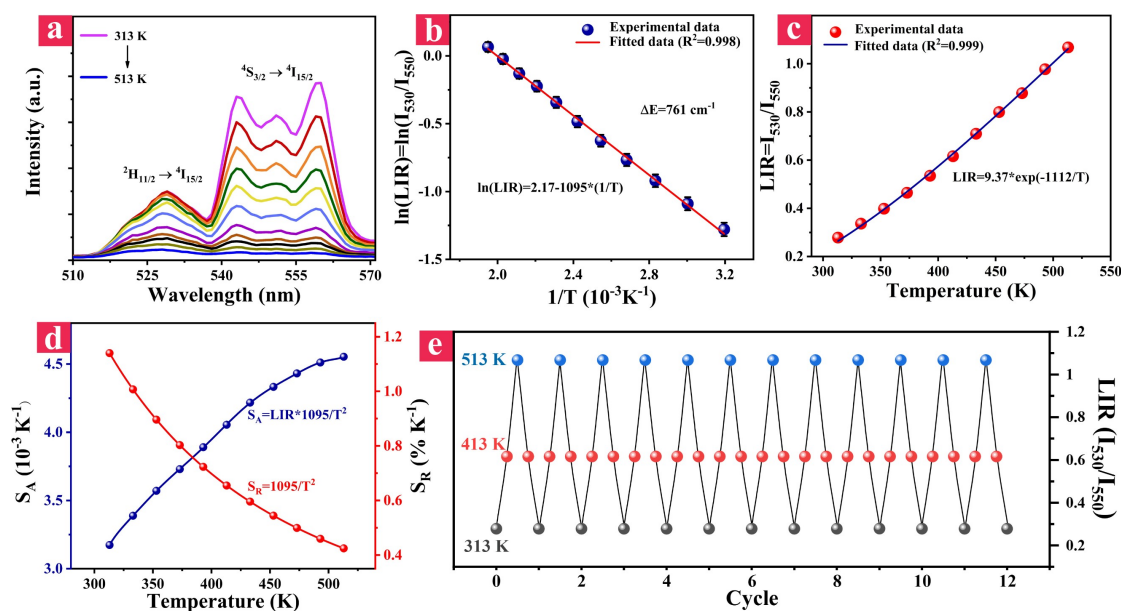
Figure 6. Temperature detection properties based on the upconversion emission. (a) Temperature dependent upconversion luminescent spectra of the CaZnOS:Mn^{2+}/Er^{3+} between the temperature range of 313-513 K upon 980 nm excitation. (b) Plot of $\ln(I_{530}/I_{550})$ versus the inverse absolute temperature ($1/T$) in the heating process. (c) Luminescence intensity ratio (LIR) versus the absolute temperature, presenting an exponential relationship. (d) The absolute and relative sensitivity of the material. (e) The repeatability test.

Real-time and accurate temperature detection is of great importance in modern society. In particular, the optical temperature sensing based on the LIR technique possesses self-referenced property. It can achieve non-contact and remote detection of temperature in a complex and

16

harsh electromagnetic environment. Figure 6a demonstrates the upconversion luminescent spectra of CaZnOS:Mn^{2+}/Er^{3+} sample as a function of temperature from 313 to 513 K under excitation of 980 nm laser. With the temperature increasing, the upconversion emitting intensity decreases gradually because of the thermal quenching effect. Meanwhile, the emitting peaks located at 530 and 550 nm generated from $^2H_{11/2}{\rightarrow}^4I_{15/2}$ and $^4S_{3/2}{\rightarrow}^4I_{15/2}$ transitions present quite different decay trends. Obviously, the upconversion luminescent decay rate from $^2H_{11/2}{\rightarrow}^4I_{15/2}$ transition is slower than that $^4S_{3/2}{\rightarrow}^4I_{15/2}$ transition. In other words, the emission intensities of the sample are extremely dependent on the temperature, owing to the thermal coupling levels $^2H_{11/2}$ and $^4S_{3/2}$ of Er^{3+}. Then we should know that the LIR technology for measuring temperature is based on the two green upconversion emissions generated by $^2H_{11/2}{\rightarrow}^4I_{15/2}$ and $^4S_{3/2}{\rightarrow}^4I_{15/2}$ transitions. And the LIR of the two bands varies, which is regularly caused by the enhancements of nonradiative relaxation, endowing the material with the capability of temperature sensing.[17] Theoretically, due to the energy gap (ΔE) between the $^2H_{11/2}$ and $^4S_{3/2}$ energy levels is small, the relative population of the two close levels achieves the thermal equilibrium quickly. And it follows the Boltzmann distribution at a certain temperature.[52] Thus, the intensity of luminescence is proportional to the population of the relevant energy levels, which can be expressed by Equation 2:

$$LIR = \frac{I_{530}}{I_{550}} = \frac{g_H A_H h \upsilon_H}{g_S A_S h \upsilon_S} \exp(-\frac{\Delta E}{kT}) = B \exp(-\frac{\Delta E}{kT}) \qquad (2)$$

Where I_{530} and I_{550} are the upconversion luminescence integral intensities of the $^2H_{11/2}{\rightarrow}^4I_{15/2}$ and $^4S_{3/2}{\rightarrow}^4I_{15/2}$ transitions, respectively. g_H and g_S are the degeneracy of the $^2H_{11/2}$ and $^4S_{3/2}$ energy state; A_H (υ_H) and A_S (υ_S) indicate to the spontaneous emission rate (frequency) of $^2H_{11/2}$, $^4S_{3/2}{\rightarrow}^4I_{15/2}$ transition. h is the Planck constant; T is the absolute temperature of thermal equilibrium; k is the Boltzmann constant; ΔE is the energy gap between the two thermally coupled energy levels $^2H_{11/2}$ and $^4S_{3/2}$. B is the temperature-independent scaling constant.

The natural logarithm of Equation 1 shows that $ln(LIR)$ and the reciprocal of absolute temperature ($1/T$) satisfy the following relationship:

$$\ln(LIR) = \ln(B) - \frac{E}{k} \times \frac{1}{T}$$

(3)

Figure 6b shows the plot of $ln(I_{530}/I_{550})$ versus the inverse absolute temperature ($1/T$) during the heating process. The energy difference ΔE (761 cm^{-1}) has been calculated by fitting experiment data and Equation 3. And the fitting quality is high as $R^2 = 0.998$. Figure 6c presents the relationship between LIR versus the absolute temperature, showing an excellent exponential relationship with a high fitting quality $R^2 = 0.999$. As we all know, the quite significant parameter used to evaluate the performance of optical temperature measuring material is temperature sensitivity. It includes the absolute sensitivity (S_A) and the relative sensitivity (S_R). The S_A is defined as the variation of LIR when the temperature varies by 1 K. The S_R means to the normalized absolute temperature sensitivity relative to the LIR, which can be used to fairly evaluate the temperature sensing capability of different systems. Their expressions are as follows:

$$S_A = \left| \frac{\partial LIR}{\partial T} \right| = LIR \xi \frac{\Delta E}{kT^2}$$

(4)

$$S_R = \left| \frac{1}{LIR} \frac{\partial LIR}{\partial T} \right| \xi 100\% = \frac{\Delta E}{kT^2} \xi 100\%$$

(5)

Figure 6d demonstrates the variation of the S_A and S_R value with the temperature from 313 to 513 K. And the S_A value gradually increases with the temperature from 3.2×10^{-4} K^{-1} at 313 K to the maximum 4.5×10^{-3} K^{-1} at 513 K. And in the researched temperature region (313-513 K), the maximum S_R value reaches 1.14% K^{-1} at 313 K. Meanwhile it decreases with the temperature rising from 313 to 513 K. Besides, the repeatability test has been conducted by 12 cycles. Figure 6e shows that the sample has excellent stability. These results indicate that the optical material has good temperature sensing capability.

3. Conclusions

In summary, the smart optical materials have been successfully synthesized by doping transition metal Mn^{2+} and lanthanide Er^{3+} into quaternary piezoelectric MZnOS (M=Ca, Sr, Ba) microcrystals with the solid-state reaction. The optical sensing properties of quaternary piezophotonic materials are systematically investigated. The XRD and SEM measurements indicate that the microcrystals have been fabricated with highly crystalline. The EDS and XPS results suggest that Mn^{2+} and Er^{3+} ions are homogeneously distributed into microcrystals. In addition, the PL and ML spectra show that the prepared samples can realize energy conversion under multi-mode stimuli, such as UV light, 980 nm laser, and stress. These quaternary piezoelectric semiconductors with wide band gaps can efficiently convert mechanical energy into light emission. More importantly, the microcrystals can not only measure stress/strain but also detect the temperature in a non-contact and real-time way. Specifically, the flexible composite films were prepared by mixing ML particles and polymers. They can be used for recording handwriting and anti-counterfeiting by visualizing the pressure intensity distribution. Besides, for the purpose of obtaining a stress sensor that can be used to analyze large strain/stress distribution, the composite blocks were fabricated by mixing ML particles and epoxy resin. And according to the experimental results, the sensors (MZnOS:Mn^{2+}/Er^{3+}, M=Ca, Sr, Ba) have a low response threshold and high temperature sensitivity. It shows that the luminescent ions doped quaternary piezoelectric materials may have promising applications in advanced optical sensors.

Supporting Information

Supporting Information is available from the Wiley Online Library or from the author.

Acknowledgements

References

[1] J. H. Hao, C. N. Xu, *MRS Bull*. **2018**, *43*, 965.

[2] J. Li, D. F. Peng, R. R. Bao, M. Dong, S. Fu, C. F. Pan, *Appl. Phys. Rev*. **2020**, *7*, 011404.

[3] J. Lin, Y. Zhou, Q. Lu, X. Wu, C. Lin, T. Lin, K. Xue, X. Miao, B. Sa, Z. Sun, *J. Mater. Chem. A* **2019**, *7*, 19374.

[4] G. X. Bai, M. K. Tsang, J. H. Hao, *Adv. Opt. Mater*. **2015**, *3*, 431.

[5] L. Chen, M. C. Wong, G. X. Bai, W. J. Jie, J. H. Hao, *Nano Energy* **2014**, *14*, 372.

[6] M. C. Wong, L. Chen, M. K. Tsang, Y. Zhang, J. H. Hao, *Adv. Mater*. **2015**, *27*, 4488.

[7] M. C. Wong, L. Chen, G. X. Bai, B. L. Huang, J. H. Hao, *Adv. Mater*. **2017**, 1701945.

[8] X. F. Wang, R. M. Yu, C. Y. Jiang, W. G. Hu, W. Z. Wu, Y. Ding, W. B. Peng, S. Li, Z. L. Wang, *Adv. Mater*. **2016**, *28*, 7234.

[9] J. C. Zhang, C. Pan, Y. F. Zhu, L. Z. Zhao, H. W. He, X. F. Liu, J. R. Qiu, *Adv. Mater*. **2018**, 1804644.

[10] B. L. Huang, D. F. Peng, C. F. Pan, *Phys. Chem. Chem. Phys*. **2017**, *19*, 1190.

[11] J. C. Zhang, X. S. Wang, G. Marriott, C. N. Xu, *Prog. Mater. Sci*. **2019**, *103*, 678.

[12] J. Y. Zhou, Y. Gu, J. Y. Lu, L. D. Xu, J. C. Zhang, D. Wang, W. X. Wang, *Chem. Eng. J*. **2020**, *390*, 124473.

[13] Y. Fujio, C. N. Xu, Y. Terasawa, Y. Sakata, J. Yamabe, *Int. J. Hydrogen Energ*. **2016**, *41*, 1333.

[14] X. D. Wang, D. F. Peng, B. L. Huang, C. F. Pan, Z. L. Wang, *Nano Energy* **2019**, *55*, 389.

[15] D. Tu, C. N. Xu, A. Yoshida, M. Fujihala, J. Hirotsu, X. G. Zheng, *Adv. Mater*. **2017**, *29*, 1606914.

[16] D. F. Peng, Y. Jiang, B. L. Huang, F. Wang, *Adv. Mater*. **2020**, 1907747.

[17] J. J. Guo, B. Q. Zhou, C. X. Yang, Q. H. Dai, L. J. Kong, *Adv. Funct. Mater*. **2019**, 1902898.

[18] T. Q. Trung, T. M. L. Dang, S. Ramasundaram, P. T. Toi, S. Y. Park, N. E. Lee, *ACS Appl. Mater. Inter*. **2019**, *11*, 2317.

[19] J. Guo, X. Liu, N. Jiang, A. K. Yetisen, H. Yuk, C. Yang, A. Khademhosseini, X. Zhao, S. H. Yun, *Adv. Mater*. **2016**, *28*, 10244.

[20] H. Zou, X. Q. Yang, B. Chen, Y. Y. Du, B. Y. Ren, X. W. Sun, Q. W. Zhang, F. Wang, *Angew. Chem. Int. Edit*. **2019**, *58*, 17255-17259.

[21] D. Tu, W. Zheng, P. Huang, X. Chen, Coord. *Chem. Rev*. **2019**, *378*, 104.

[22] X. Cheng, Y. Pan, Z. Yuan, X. Wang, W. Su, L. Yin, X. Xie, L. Huang, *Adv. Funct. Mater*. **2018**, *28*, 1800208.

[23] Y. H. Cheng, J. G. Wang, Z. J. Qiu, X. Y. Zheng, B. Z. Tang, *Adv. Mater*. **2017**, *29*, 1703900.

[24] Z. L. Wang, *Nano Today* **2010**, 5, 540

[25] Z. L. Wang, *J. Phys. Chem. Lett*. **2010**, 1, 1388.

[26] L. J. Li, K. L. Wong, P. F. Li, M. Y. Peng, *J. Mater. Chem. C* **2016**, *4*, 8166.

[27] Y. Y. Du, Y. Jiang, T. Y. Sun, J. X. Zhao, B. L. Huang, D. F. Peng, F. Wang, *Adv. Mater*. **2019**, *31*, 1807062.

[28] J. C. Zhang, L. Z. Zhao, Y. Z. Long, H. D. Zhang, B. Sun, W. P. Han, X. Yan, X. S. Wang, *Chem. Mater*. **2015**, *27*, 7481.

[29] R. I. Gulyaeva, E. N. Selivanov, A. D. Vershinin, V. M. Chumarev, *Inorg. Mater*. **2006**, *42*, 897.

[30] Z. Long, Y. Wen, J. Zhou, J. Qiu, H. Wu, X. Xu, X. Yu, D. Zhou, J. Yu, Q. Wang, *Adv. Opt. Mater*. **2019**, *7*, 1900006.

[31] Y. Zhou, Y. L. Yang, Y. T. Fan, W. Yang, W. B. Zhang, J. F. Hu, Z. J. Zhang, J. T. Zhao, *J. Mater. Chem. C* **2019**, *7*, 8070.

[32] D. Tu, C. N. Xu, Y. Fujio, A. Yoshida, *Light: Sci. Appl*. **2015**, *4*, e356.

[33] W. Liu, K. T. Lai, K. Eckhardt, Y. Prots, U. Burkhardt, M. Valldor, *J. Solid State Chem*. **2017**, *246*, 225.

[34] S. Broadley, C. F. Smura, S. J. Clarke, *Inorg. Chem*. **2005**, *44*, 9092.

[35] B. P. Chandra, V. K. Chandra, P. Jha, *Phys. B* **2015**, *463*, 62.

[36] G. X. Bai, S. G. Yuan, Y. D. Zhao, Z. B. Yang, S. Y. Choi, Y. Chai, S. F. Yu, S. P. Lau, J. H. Hao, *Adv. Mater*. **2016**, *28*, 7472.

[37] N. Guerfi, T. A. Nguyen Tan, J. Y. Veuillen, D. B. Lollman, *Appl. Surf. Sci*. **1992**, *56*, 501.

[38] Y. J. Zhao, G. X. Bai, Y. J. Hua, Q. H. Yang, L. Chen, S. Q. Xu, *J. Lumin*. **2020**, *221*, 117037.

[39] B. Guan, H. Lin, Z. Huang, *Chem. Eng. Sci*. **2018**, *189*, 320.

[40] M. E. Becerra, N. P. Arias, O. H. Giraldo, A. B. López, *Catal. Today* **2011**, *281*, 460.

[41] S. Liu, X. Wu, D. Weng, M. Li, H. R. Lee, *Chem. Eng. J*. **2012**, *203*, 25.

[42] R. N. Bhargava, D. Gallagher, X. Hong, A. Nurmikko, *Phys. Rev. Lett*. **1994**, *72*, 416.

[43] G. X. Bai, M. K. Tsang, J. H. Hao, *Adv. Funct. Mater*. **2016**, *26*, 6330.

[44] H. L. Zhang, D. F. Peng, W. Wang, L. Dong, C. F. Pan, *J. Phys. Chem. C* **2015**, *119*, 28136.

[45] F. Wang, R. R. Deng, J. Wang, Q. X. Wang, Y. Han, X. Y. Chen, X. G. Liu, *Nat. Mater*. **2011**, *10*, 968.

[46] C. Wu, S. S. Zeng, Z. F. Wang, F. Wang, H. Zhou, J. C. Zhang, Z. P. Ci, L. Y. Sun, *Adv. Funct. Mater*. **2018**, 1803168.

[47] Y. X. Zhuang, D. Tu, C. J. Chen, L. Wang, H. W. Zhang, H. Xue, C. H. Yuan, G. R. Chen, C. F. Pan, L. Z. Dai, R. J. Xie, *Light: Sci. Appl*. **2020**, *9*, 182.

[48] T. Jiang, Y. F. Zhu, J. C. Zhang, J. J. Zhu, M. Zhang, J. R. Qiu, *Adv. Funct. Mater*. **2019**, 1906068.

[49] X. D. Wang, H. L. Zhang, L. Dong, D. F. Peng, C. F. Pan, Z. L. Wang, *Adv. Mater*. **2015**, *27*, 2324.

[50] X. Qian, Z. R. Cai, M. Su, F. Y. Li, W. Fang, C. F. Pan, Y. L. Song, *Adv. Mater*. **2018**, *30*, 1800291.

[51] X. Y. Wei, X. Wang, S. Y. Kuang, L. Su, H. Y. Li, Y. Wang, C. Pan, Z. L. Wang, G. Zhu, *Adv. Mater*. **2016**, *28*, 6656.

[52] G. J. Gao, D. Busko, S. Kauffmann-Weiss, A. Turshatov, I. A. Howard, B. S. Richards, *J. Mater. Chem. C* **2018**, *6*, 4163.

Yingjie Zhao, Dengfeng Peng, Gongxun Bai*, Youqiang Huang, Shiqing Xu*, Jianhua Hao*

Multi-Responsive Emissions in Luminescent Ions Doped Quaternary Piezophotonic Materials for Mechanical-to-Optical Energy Conversion and Sensing Applications
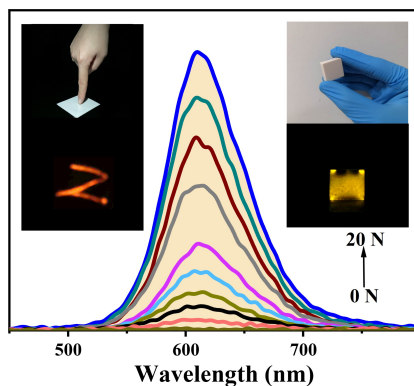
The efficient multimode luminescence can be achieved by codoping transition metal and lanthanide ions into the host lattice of quaternary piezophotonic semiconductors MZnOS (M=Ca, Sr, Ba). They can simultaneously respond to ultraviolet, NIR laser and force, and generate completely different optical signal, which can be used for optical sensing of stress and temperature.

Supporting Information

Multi-Responsive Emissions in Luminescent Ions Doped Quaternary Piezophotonic Materials for Mechanical-to-Optical Energy Conversion and Sensing Applications

Yingjie Zhao, Dengfeng Peng, Gongxun Bai*, Youqiang Huang, Shiqing Xu*, Jianhua Hao*

Experimental section

ML microcrystals synthesis and device preparation: All the MZnOS:Mn^{2+}/Er^{3+} (M=Ca, Sr, Ba) microcrystals were prepared by solid-state reaction way in a vacuum furnace. The raw materials include $CaCO_3$ (99.99%, Sinopharm Group Co. Ltd.), $BaCO_3$ (99.99%, Aladdin), $SrCO_3$ (99.99%, Aladdin), ZnS (99.99%, Aladdin), $MnCO_3$ (99.99%, Sinopharm Group Co. Ltd.) and ErF_3 (99.99%, Aladdin). All the samples with nominal composition of $M_{1-y}Zn_{1-x}OS:xMn^{2+}$/$yEr^{3+}$ (M=Ca, Sr, Ba, x=0.02, y=0.02). In the synthesis of Mn^{2+}/Er^{3+} codoped MZnOS (M=Ca, Sr, Ba), the weighted raw materials were homogeneously mixed and the mixtures were sintered at 1100 °C, 1050 °C, 1020 °C for 4 hours, respectively. Then, the sintered samples were naturally cooled down to room temperature and subsequently grounded into powders for application and characterization. To make the composite flexible ML film, as-prepared ML particles (0.6 g) were mixed with PDMS (0.2 g) and sealed homogeneously between two squared by polyethylene glycol terephthalate (PET) sheets (4.0 cm×4.0 cm). For the fabrication of composite ML block, as-prepared ML particles (1.0 g) were fully mixed with epoxy resin (1.0 g) and poured into a mold, heating under 80 °C for 4 hours.

Sample characterization: The X-ray diffraction (XRD) patterns were recorded by a Bruker D2 phase X-ray diffraction analyzer with Cu-Kα (1.5406 Å) radiation. The X-ray photoelectron spectroscopy (XPS) spectra of the materials were detected by an Escalab 250Xi spectrometer. For analyzing the surface micromorphology and the elemental distribution of the as-prepared

samples, the scanning electron microscope (SEM) and the energy disperse spectroscopy (EDS) data were obtained by a Hitachi SU8010 field-emission scanning microscope equipped with an energy-dispersive X-ray spectroscope analyzer. Photoluminescence (PL) and temperature dependent upconversion spectra were recorded by using a HORIBA QM8075-11 spectrophotometer equipped with a photomultiplier R13456 detector. The diffuse reflectance spectra were obtained by a Shimadzu UV-3600 UV-vis spectrophotometer. In addition, an Ocean Optics QE Pro fiber spectrometer was used to record the ML spectra in the research. An AIPU SH-200N digital force gauge and a Shimadzu AGS-X universal testing machine were used to measure the ML properties. A smart phone was used to take the long-exposure photos for analyzing the pressure distribution of the samples.
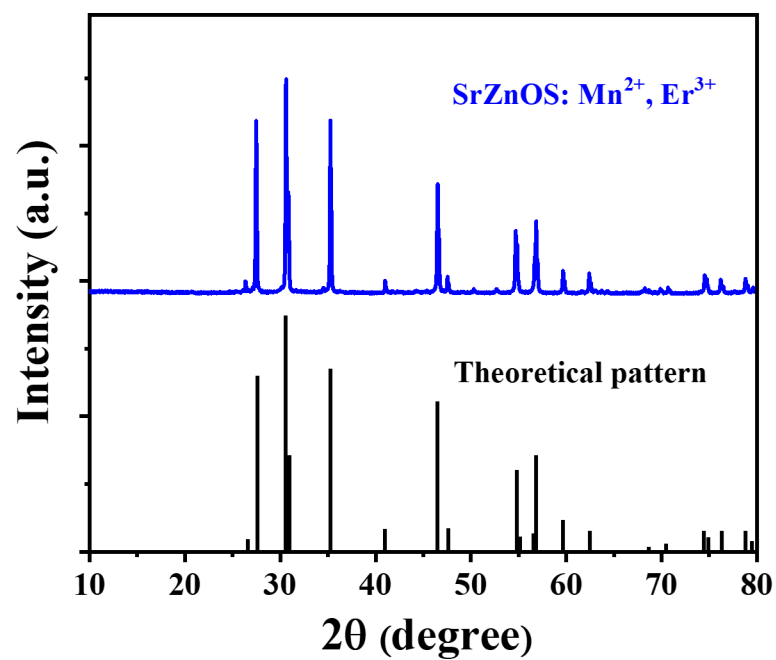
**Figure S1** XRD pattern of SrZnOS:Mn^{2+}/Er^{3+} sample and the SrZnSO theoretical pattern (ICSD #431819).
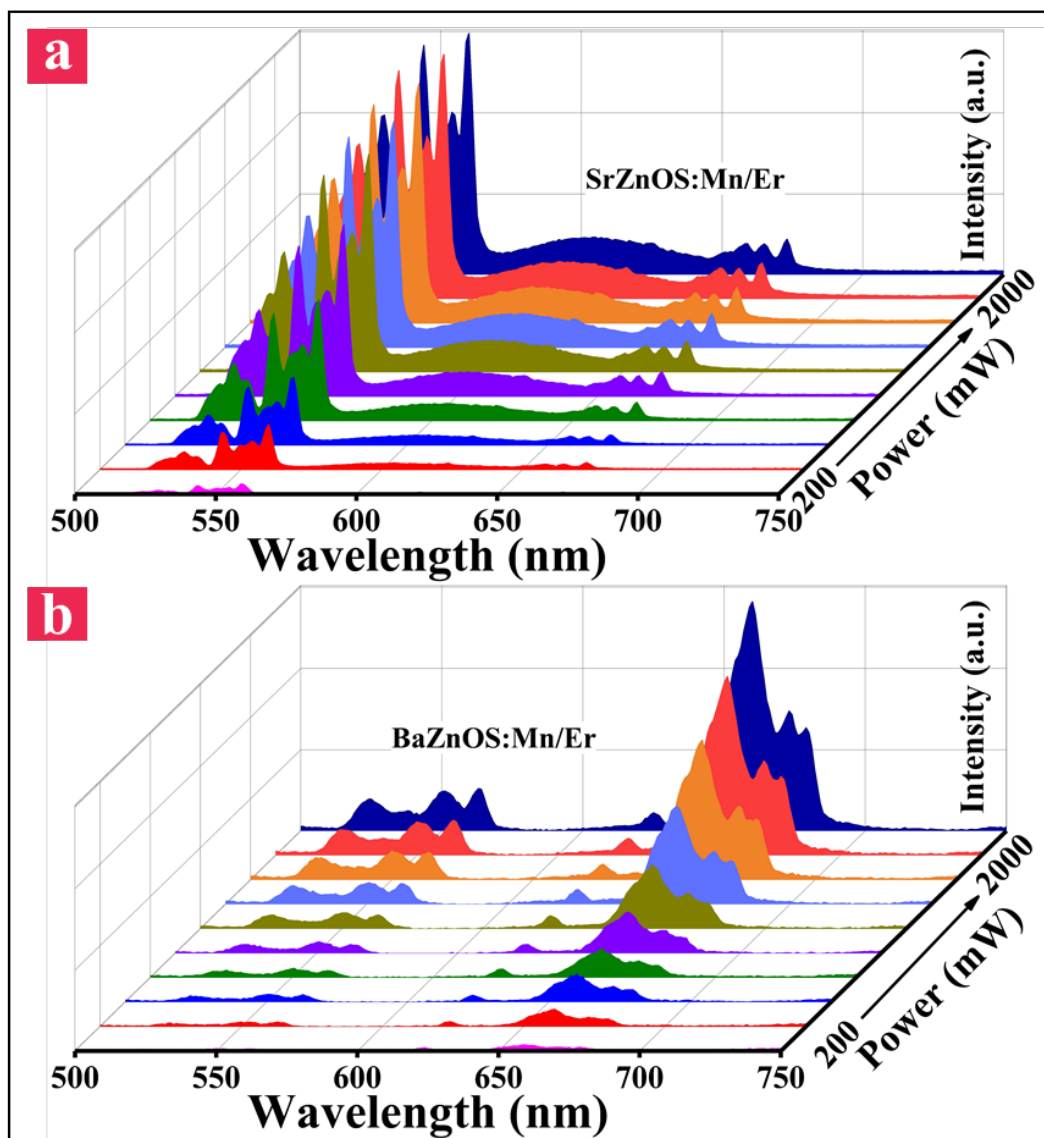
Figure S2 Upconversion emission spectra of SrZnOS:Mn^{2+}/Er^{3+} and BaZnOS:Mn^{2+}/Er^{3+}

powders under the 980 nm laser with different pump power (200-2000 mW).
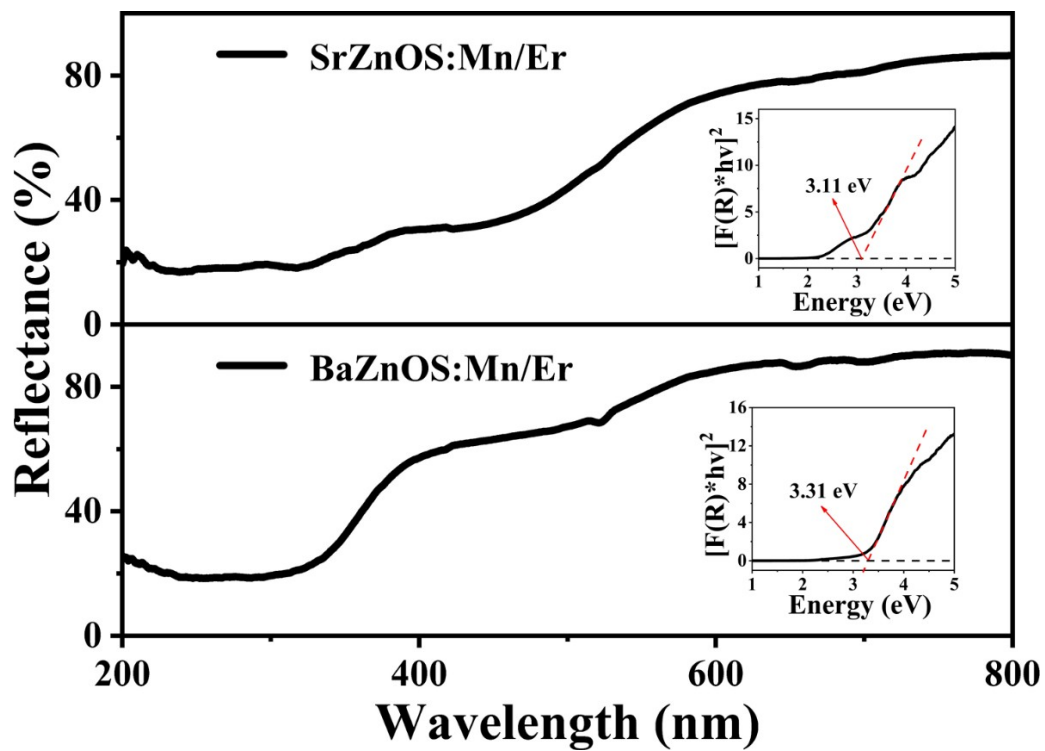
Figure S3 The diffuse reflectance spectra of the doped SrZnOS and BaZnOS. The insets depict the Tauc plots and the estimated band gap for the doped SrZnOS and BaZnOS, respectively.
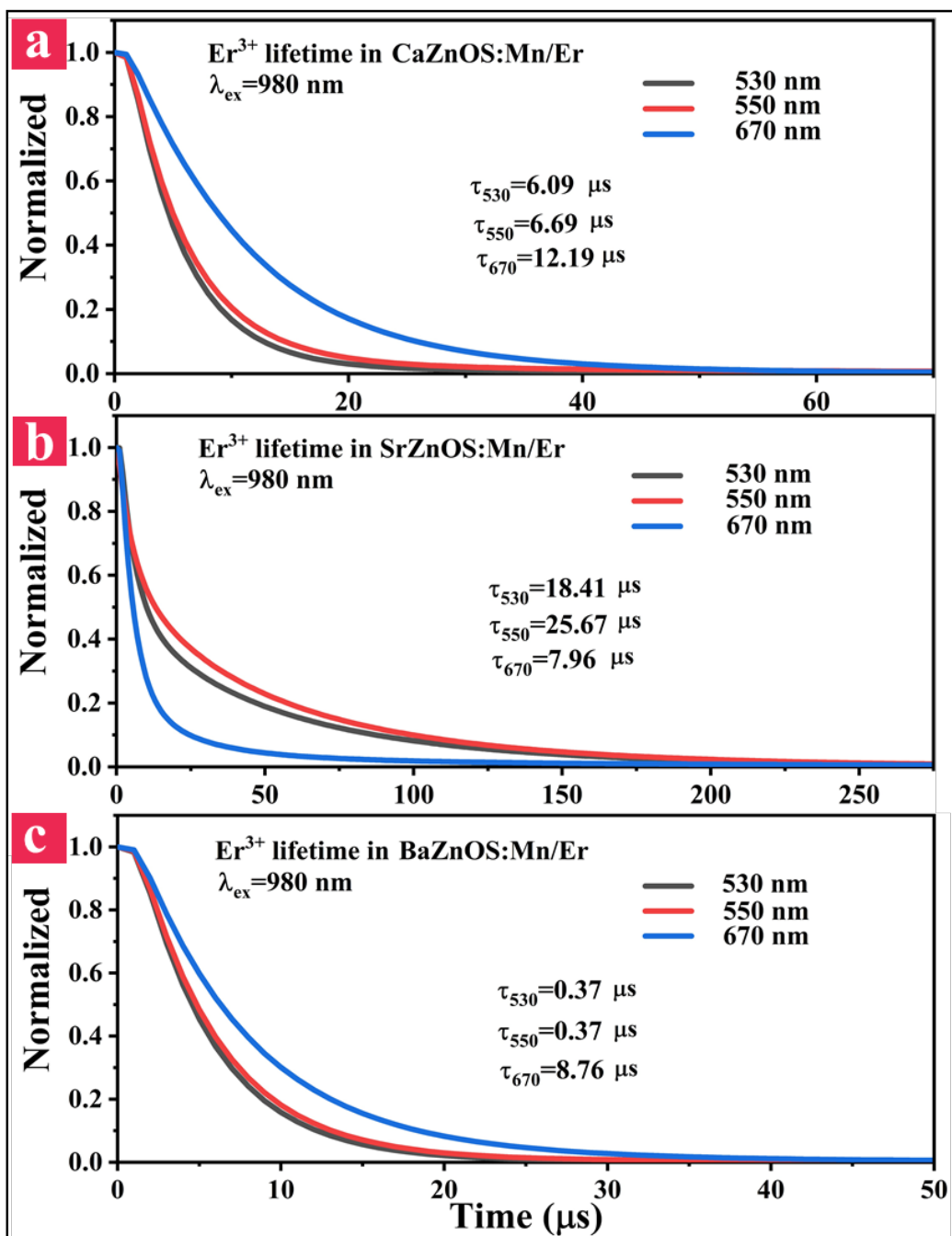
Figure S4 Decay curves of Er³⁺ upconversion emission at 530, 550, and 670 nm under excitation at 980 nm in different hosts.
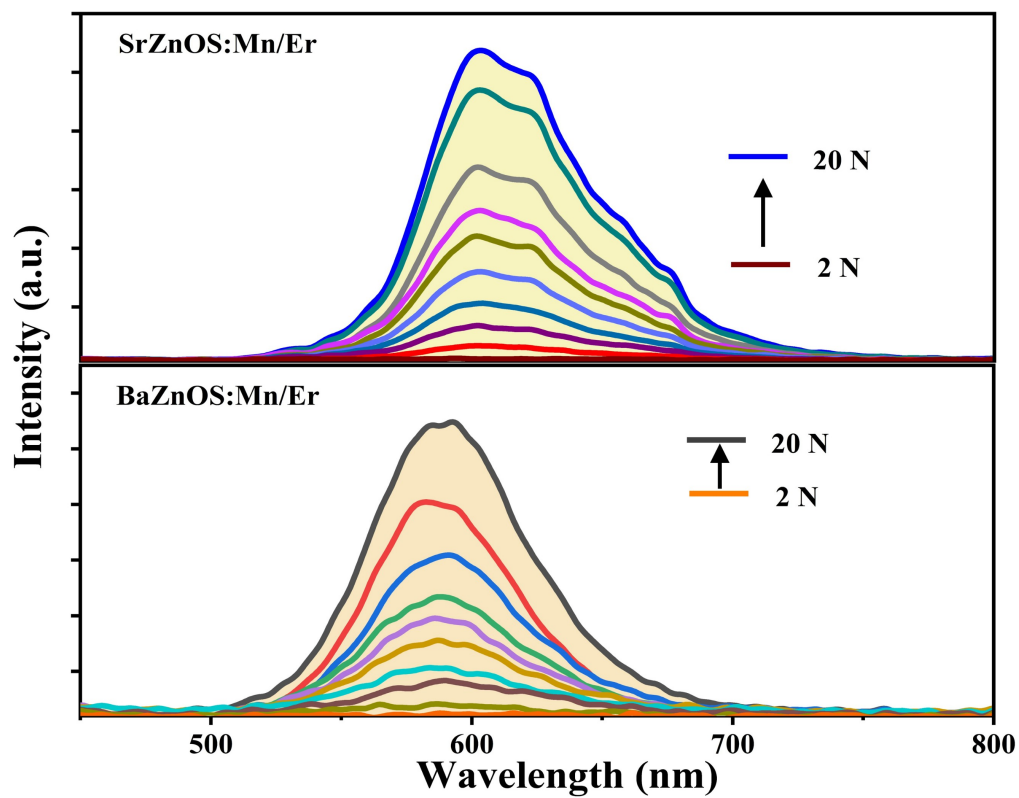
Figure S5 ML spectra of the SrZnOS:Mn^{2+}/Er^{3+} and BaZnOS:Mn^{2+}/Er^{3+} composite films under various applied forces.